

# Toward thermoelectric characterization of (nano)materials by in situ transmission electron microscopy

Simon Hettler\* Mohammad Furqan Andrés Sotelo Raul Arenal\*

Dr. S. Hettler, M. Furqan, Dr. A. Sotelo, Dr. R. Arenal  
Instituto de Nanociencia y Materiales de Aragón (INMA), CSIC-Universidad de Zaragoza, 50009 Zaragoza, Spain

Email Address: hettler@unizar.es, arenal@unizar.es

Dr. S. Hettler, M. Furqan, Dr. R. Arenal

Laboratorio de Microscopías Avanzadas (LMA), Universidad de Zaragoza, 50018 Zaragoza, Spain

Dr. R. Arenal

ARAID Foundation, 50018 Zaragoza, Spain

Keywords: *in-situ transmission electron microscopy, measurement on individual nanomaterial, sample preparation, electrical properties, focused ion beam*

Keywords: *in situ transmission electron microscopy, seebeck coefficient, thermoelectricity, nanomaterial*

We explore the possibility to perform an in situ transmission electron microscopy (TEM) thermoelectric characterization of materials. A differential heating element on a custom in situ TEM microchip allows to generate a temperature gradient across the studied materials, which are simultaneously measured electrically. A thermovoltage was induced in all studied devices, whose sign corresponds to the sign of the Seebeck coefficient of the tested materials. The results indicate that in situ thermoelectric TEM studies can help to profoundly understand the interplay between the thermoelectric properties on one side and the structure/composition of the materials down to the atomic level on the other side, including grain boundaries, dopants or crystal defects. We propose an improved in situ TEM microchip design, which should facilitate a full quantitative measurement of the induced temperature gradient, the electrical and thermal conductivities, as well as the Seebeck coefficient.

## 1 Introduction

Thermoelectric materials are an important building block for generation of green energy from heat and a huge range of different materials are being studied [1, 2, 3, 4]. In general, the thermoelectric effect is a complex phenomenon and the Seebeck coefficient strongly depends on crystallinity, presence of dopants, contaminants or impurities in the material [5, 6, 7]. In the development of thermoelectric bulk materials, different strategies are followed to improve the figure of merit,  $ZT$ , including grain-boundary engineering [6] or doping [7]. Nanomaterials, nano-composites or nano-structured devices are also promising candidates for thermoelectric materials [8, 9, 5]. The miniaturization of devices, the use of nanomaterials and the complex interplay between the structure/composition of materials and their thermoelectric properties have led to numerous different approaches for thermoelectric characterization of (nano)materials [10, 11, 12, 13].

Transmission electron microscopy (TEM), combined with related spectroscopic techniques, allows the in-depth analysis of structure and composition down to the atomic scale [14, 15]. Technological developments have improved the energy resolution in electron energy-loss spectroscopy (EELS) and allow the local study of phonons by scanning (S)TEM [16, 17], which are important for heat transport phenomena. Recently, in situ TEM studies have gained significant importance as they allow to study the evolution of materials under external stimuli. One branch of in situ experiments are electrical studies, where the influence of an applied voltage [18, 19, 20] or current [21] on a material is investigated. Here, we explore the possibility to measure the Seebeck coefficient and thermoelectric properties of materials, including individual nanomaterials, by in situ TEM. The combination of thermoelectric characterization and TEM is promising for gaining a deeper understanding of fundamental processes in thermoelectric materials as, for example, the role of grain boundaries.

## 2 Results and discussion

### 2.1 Device setup

The general concept to measure the Seebeck coefficient is to generate a temperature gradient along the material to be studied and simultaneously measure the generated electrical potential. To combine such a measurement with TEM investigations, a microchip that fits in an in situ TEM sample holder was designed and fabricated by microelectromechanical systems (MEMS) technologies. Chip fabrication is described in detail in the experimental section. **Figure 1** shows a photograph, an optical microscopy image and a scanning electron microscopy (SEM) image of one of these chips, which consist of a differential heating device and two contact pads (10 nm Ti + 150 nm Pt) on top of a free-standing low-stress silicon nitride membrane (thickness 1  $\mu\text{m}$ ). The differential heating device is located on one side of the membrane in order that an applied heating current ( $I_H$ ) would create a temperature gradient between the contact pads, which are located in the center of the membrane. The polarity of the voltage applied to the device is indicated in Figure 1c.

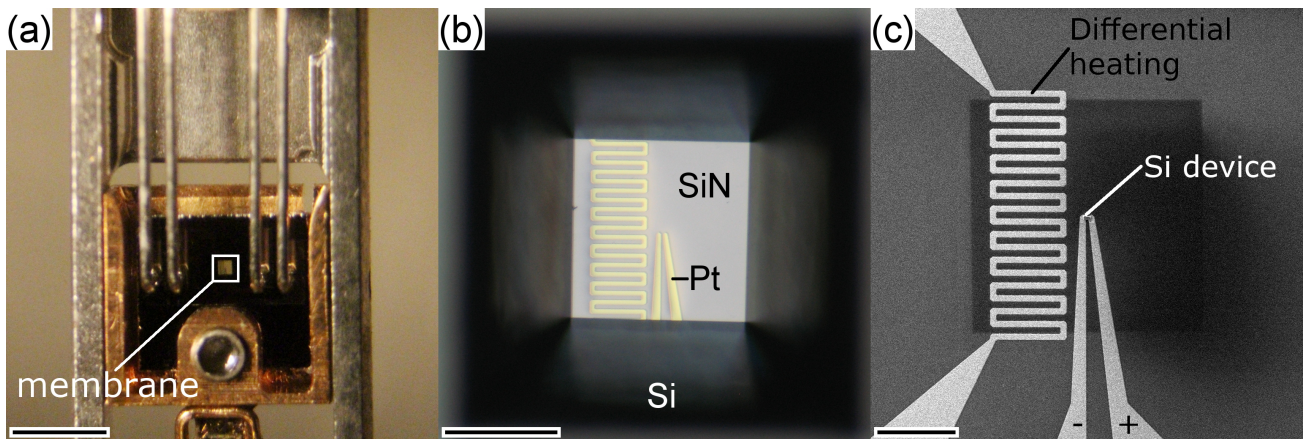


Figure 1: (a) Photograph of the tip of the in situ TEM holder with thermoelectric microchip inserted. The position of the membrane has been indicated. (b) Optical microscopy image from the membrane with heating device and contact pads taken from the back side of the in situ TEM microchip. (c) SEM image taken from the front side of the Si device. Polarity of the I-V measurements of the devices is indicated. Scale bars are (a) 2 mm, (b) 200  $\mu\text{m}$  and (c) 100  $\mu\text{m}$ .

We studied five different thermoelectric devices with the fabricated chips. Four devices were prepared from bulk samples: a standard p-doped (boron) silicon single crystal, single-crystalline molybdenum (source: sputter target, structural analysis in supplementary information (SI), section SI1) and a strontium-doped calcium cobaltite (CCO:  $\text{Ca}_{2.93}\text{Sr}_{0.07}\text{Co}_4\text{O}_9$ ) misfit-layered compound (MLC). For the CCO material, two devices were fabricated with different crystal orientation as discussed below. The fifth device is a nanotube (NT) based on the MLC  $(\text{LaS})_{1.14}\text{-TaS}_2$  [22]. In order to study these materials, a piece of each has to be deposited between the two contact pads on the in situ TEM chip. As detailed in the experimental section, the focused ion beam (FIB) technique was used to prepare the devices. Two different approaches have been employed for bulk [23] and NT devices [24], respectively.

### 2.2 Reference materials and device characterization

**Figure 2a** shows a SEM image of the prepared p-doped Si device, where the material was cut into a cuboid with defined geometry in the central area above the hole in the membrane. The crystal orientation is 100 in vertical direction and approximately 032 in direction of the current flow between the contacts (SAED analysis in SI2). Energy-dispersive X-Ray spectroscopy (EDX) indicates a minor surface oxidation and Ga incorporation (SI3). Figure 2b depicts an I-V characterization of the device shown in (a) obtained at different applied heating currents  $I_H$  between 0.1 (blue curve) and 5 mA (red curve). With increasing  $I_H$  applied to the differential heating device, the I-V curve shifts along the x-axis and the gradient slightly increases. The gradient change is linked to a slight decrease in average resistance

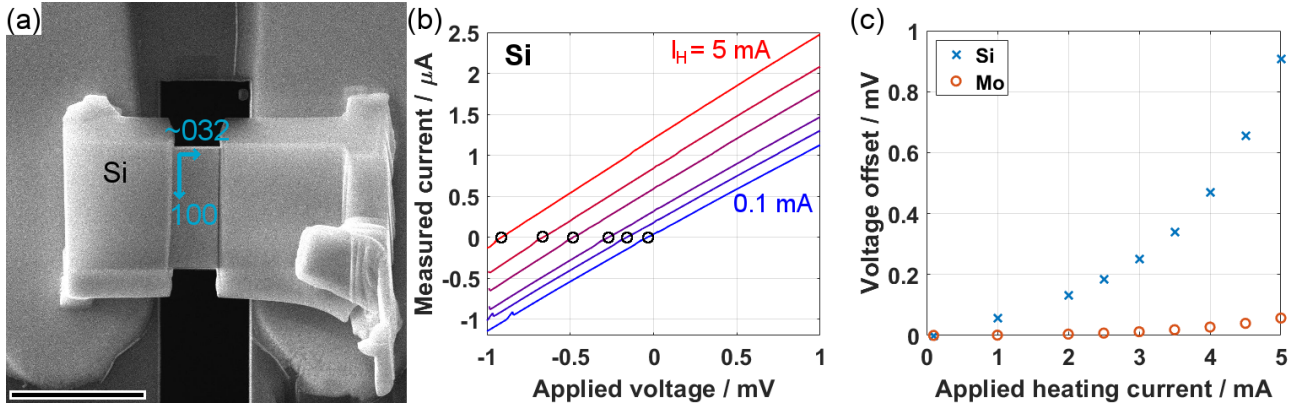


Figure 2: (a) SEM image of the fabricated device showing the Si sheet deposited between the contact pads of the in situ chip. Orientation of the Si crystal lattice is indicated. Scale bar is 5  $\mu\text{m}$ . (b) I-V characterization of the device for  $I_H = 0.1$  (blue), 2, 3, 4, 4.5 and 5 mA (red). (c) Plot of voltage offset depending on  $I_H$  for the Si device shown in (a) and a similar device prepared from single-crystalline Mo.

from 890  $\Omega$  to 775  $\Omega$  due to an increase in temperature and a related improvement of the semiconducting Si and also likely due to a reduction of contact resistance. The shift can be attributed to the generation of a voltage induced by a temperature gradient along the sample. To measure this shift, a linear regression  $I(V) = -V/R + I_0$  is performed on the I-V curves and the shift is calculated from  $V_0 = -\frac{I_0}{R}$  and is marked by black circles in Figure 2b. The negative sign is due to the employed polarity (Figure 1c), as the temperature gradient is opposite to the applied voltage. The voltage offset is determined by the value of  $V_0(I_H)$  relative to  $V_0(I_H=0)$  to account for possible minor intrinsic currents.  $V_0$  is shown in Figure 2c in dependence of  $I_H$  for the Si device and a similar sample prepared from single-crystalline Mo (SI4). Both curves show a clear increase of the voltage offset with  $I_H$ , which corresponds with the expected increase of the temperature gradient along the material. The voltage offset is positive, which agrees with the (positive) sign of the Seebeck coefficient of both materials [25, 26]. A quantitative assessment of the measured voltages is discussed below.

To check a possible contribution to the thermoelectrical measurement by the chip itself, the raw in situ chip, without deposited material, was characterized in the same way. No measurable contribution was observed (SI5).

### 2.3 Devices made of misfit-layered compounds

**Figure 3** shows the structural analysis of the three MLC devices. Two devices were prepared from the bulk CCO material with different crystal orientations with respect to the induced temperature gradient. Two SEM images of the first CCO device before and after FIB thinning for TEM studies are shown in Figure 3a. The preparation of this device is documented in SI6. The microstructure of the Sr-doped CCO bulk material was analyzed using a standard TEM lamella (SI7), which revealed that the material possesses a micro-crystalline structure with most grains exhibiting a similar direction of the  $c$ -axis. The  $c$ -axis corresponds to the direction of the applied pressure during the hot-pressing process, see experimental section. Grain sizes are small in  $c$ -direction (approximately 500 nm) and large in  $a$ - $b$  directions (several  $\mu\text{m}$ ). A few grains and grain boundaries spanning horizontally across the device can be seen in the TEM image in Figure 3b. Figure 3c depicts a selected-area electron diffraction (SAED) pattern obtained from the thin part of the device. The SAED pattern confirms that the  $c$ -axis is perpendicular to the grain boundaries visible in Figure 3b, implying that for this device, the electrical current flow is predominantly in-plane and thus parallel to the layers of the MLC. This device is denoted as CCO || in the following. The  $c$ -axis periodicity of the CCO material is measured to be 1.07 nm from the SAED pattern, which agrees with previously reported values on bulk CCO [27].

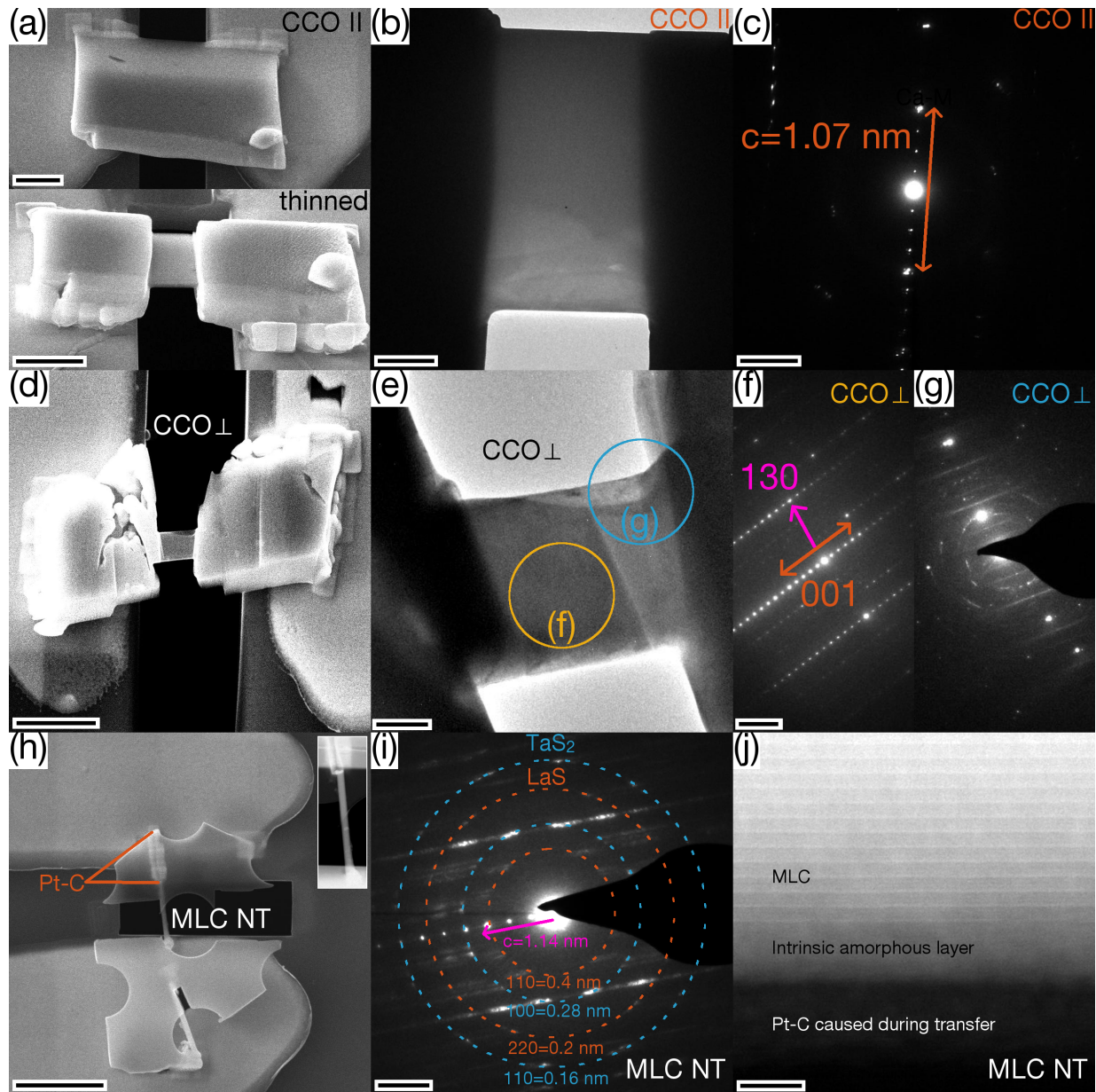


Figure 3: (a-c) Analysis of the CCO || device. (a) Two SEM images of the unthinned (top) and thinned (bottom) device, respectively. (b) TEM image of the thinned device. (c) SAED pattern acquired from the thinned sheet showing the c-axis periodicity of the MLC stack. (d-g) Analysis of the CCO  $\perp$  device. (d) SEM image. (e) TEM image of the thin part with two grains visible. (f,g) SAED patterns acquired as marked in (e). (h-j) Analysis of the MLC-NT device. (h) SEM image and inset low-magnification STEM image (height 4  $\mu\text{m}$ ). (i) SAED pattern evidencing its nanotubular structure. (j) High-angle annular dark field (HAADF) STEM image revealing the MLC stack of the NT. Scale bars are (a) 2  $\mu\text{m}$ , (b) 500 nm, (c) 3  $\text{nm}^{-1}$ , (d) 3  $\mu\text{m}$ , (e) 60 nm, (f,g) 4  $\text{nm}^{-1}$  (h) 4  $\mu\text{m}$ , (i) 1  $\text{nm}^{-1}$  and (j) 5 nm.

Figure 3d-g details a second CCO device, denoted as CCO  $\perp$ , whose preparation is shown in SI8. Figure 3d shows a SEM image of the device, which was prepared such that the current flow is roughly perpendicular to the layered structure (parallel to the *c*-axis) and that a single grain boundary falls in the thinned central part. Figure 3e shows a bright-field TEM image of this device after orientation of the left grain into a high-order zone axis (TEM stage at  $\alpha=23^\circ$ ,  $\beta=23^\circ$ ). The image clearly reveals the presence of two grains with the left grain oriented in zone-axis, appearing darker compared to the right grain. Figure 3f and 3g show two SAED patterns obtained from the left and right part of the device as marked in Figure 3e, corresponding to the two grains. The patterns confirm the orientation of the left grain in a higher-order zone-axis. An analysis of the reflections indicates the presence of [001] (1.07 nm) and [130] (0.15 nm) reflections, corresponding to a [-310] zone-axis orientation. Note that due to the monoclinic structure of the CCO material, [001] and [130] are not perpendicular to each other. On the other hand, the right grain does not exhibit a higher order orientation of the crystal with respect to the electron beam at this particular stage tilt (Figure 3g). The analysis of the device tilted to an angle where the right grain is oriented in [010] zone-axis (TEM stage at  $\alpha=16^\circ$ ,  $\beta=19^\circ$ ) is shown in SI9. As the 001 direction roughly corresponds to the  $\beta$  tilt direction, the angle between the *c*-axis directions of the two grains is estimated by the difference in  $\alpha$  tilt, which roughly corresponds to  $7^\circ$ . An EDX spectrum of this CCO device is shown in SI3 and confirms the presence of all elements of the CCO device, including the strontium doping.

The third MLC device (preparation in SI10) consists in a NT made of  $(\text{LaS})_{1.14}\text{-TaS}_2$ . A SEM image of the device is shown in Figure 3h. The silicon nitride membrane utilized for the sample transfer to the chip was milled away in the central region in order that the NT forms the only conductive connection between the contact pads. A rather long Pt-C focused ion beam induced deposition (FIBID) was needed to contact the NT to the upper contact pad. A SAED pattern acquired from the central part of the NT (Figure 3i) reveals the complex structure of the MLC NT [22]: Reflections are seen from the two different subsystems LaS (orange dashed rings) and  $\text{TaS}_2$  (blue dashed rings) and the *c*-axis periodicity of the stack (pink arrow), which is perpendicular to the NT axis, as seen in Figure 3h. The tubular structure is recognized from the streaking reflections caused by the bending of the layers. The MLC stack formed of bright  $\text{TaS}_2$  layers and LaS layers is clearly seen in a high-angle annular dark field (HAADF) STEM image (Figure 3j). Two amorphous surface layers are visible in the image. The inner, brighter part is intrinsic to the NT and was observed already prior to the transfer (SI11). The outer, dark layer was generated during the transfer process and is mainly composed of carbon and Pt stemming from the precursor gas used for the FIBID procedure employed to contact the NT. SI3 shows an STEM-EDX spectrum of the MLC-NT device confirming the expected composition.

The CCO  $\parallel$  and NT devices were analyzed (thermo)electrically similar to the Mo and Si devices (Figure 2) and the determined voltage offset  $V_0$  in dependence of  $I_H$  is shown in **Figure 4a**. The CCO  $\parallel$  device was measured twice: Firstly without thinning and still including the Pt protection cover from the TEM lamella fabrication (yellow pentagrams in Figure 4a, top image in Figure 3a) and secondly after FIB thinning (yellow crosses in Figure 4a, bottom image in Figure 3a). Only a small difference is visible between the two curves indicating that the impact on the thermoelectric effect of the Pt protection cover is small, even though it strongly contributes to the electrical conductivity of the device (see following section). Also, the thickness of the lamella (1  $\mu\text{m}$  thinned down to 350 nm in the central part) only plays a minor role as the Seebeck coefficient is a parameter mainly intrinsic to the material, which does not depend on smaller modifications of its dimensions, and if these do not affect the mixture of grains in the material. Nevertheless, the observed minor decrease of the measured voltage offset after thinning is not expected in the simple picture of an additive combination of the thermoelectric properties in a composite material. Under such an assumption, a device made of the combination of the CCO material (154  $\mu\text{V/K}$  [7]) and the Pt cover (-5  $\mu\text{V/K}$ ) should show a lower voltage than the thinned CCO material alone. However, previous studies have shown that a combination of a thermoelectric material based on cobalt oxide with a conductive metal can actually increase the Seebeck coefficient, which explains the observed trend [28, 29]. The magnitude of the voltage offset for the CCO  $\parallel$  is comparable to the Mo device, which is surprisingly low, as the Seebeck coefficient of CCO bulk material (154  $\mu\text{V/K}$ ) is

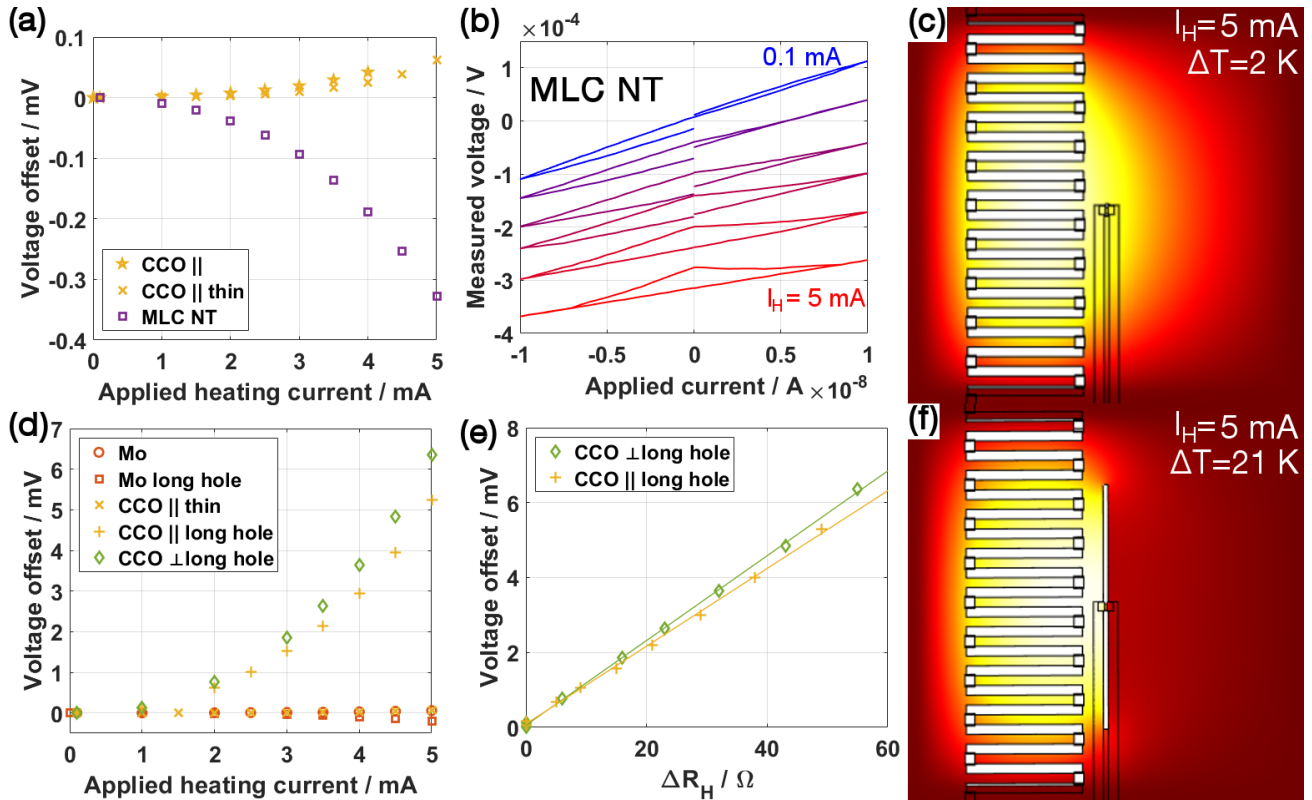


Figure 4: (a) Voltage offset for the CCO || and the MLC NT devices shown in Figure 3a-c and h-j, respectively. (b) I-V curves for the MLC NT for  $I_H = 0.1$  (blue), 2.5, 3.5, 4, 4.5 and 5 mA (red) showing a hysteresis loop. (d) Comparison of the voltage offset for Mo and CCO || devices with short and long hole together with CCO  $\perp$  device with long hole. (e) Voltage offset over resistance increase  $\Delta R$  of the heating device with linear fit. (c,f) Maps of the temperature distribution within the silicon nitride membrane obtained from COMSOL simulations assuming a (c) short and (f) long hole, respectively. White color corresponds to the maximum temperature (317 K (c) and 324 K (f)) and dark red to room temperature.

much higher than the one of Mo [26] (discussion below).

The measured voltage offset for the NT device is plotted by purple squares in Figure 4a. In contrast to the previous devices, the NT device is the only one that shows a negative voltage offset, which agrees with previous studies showing a negative Seebeck coefficient for chalcogen-based MLC materials [1]. Figure 4b shows the I-V curves for the NT device for different values of  $I_H$ . A hysteresis effect can be observed in all of the curves, which we attribute to a space-charge region formed in the long Pt-C FIBID contact. Such memristive behaviour has been frequently observed in nanoscale devices [30]. Nonetheless, the effect of the differential heating device is obvious, clearly shifting the curves in opposite direction as for the Si device. In this MLC nanotube device, only the lower, straight part of the hysteresis loop has been used to determine the voltage offset.

## 2.4 Electrical properties

In addition to the thermoelectric characterization, the chips also facilitate an in situ TEM measurement of the electrical properties of the materials. The electrical conductivity  $\sigma$  can be obtained from the measured resistance and the sample geometry. The data obtained from the devices at room temperature ( $I_H=0$ ) are summarized in SI12.

As the measurements were conducted in a two-probe setup, the contribution of contact resistance needs to be considered, which was approximately  $135 \Omega$  for the employed chips. For specimens with dimensions typical for TEM investigations, the contact resistance is only a negligible part of the total device resistance. For example, the resistance of the MLC NT with a diameter of 100 nm and a length of  $2.8 \mu\text{m}$  is  $10 \text{ k}\Omega$  and in this case, the contact resistance is only a small fraction of the total resistance. The de-

rived conductivity amounts to  $3.7 \cdot 10^4 \text{ Sm}^{-1}$ , a value which agrees with previous measurements [22, 24]. Similarly, the two thinned CCO MLC devices show resistances of  $104 \text{ k}\Omega$  (CCO  $\parallel$ ) and  $80 \text{ k}\Omega$  (CCO  $\perp$ ), which lead to conductivities of  $7 \text{ Sm}^{-1}$  and  $5 \text{ Sm}^{-1}$ , respectively. These values are of the same order of magnitude, but slightly smaller when comparing to bulk measurements [7]. This could be attributed to the fact that pores, absent in the studied microscopic devices but frequent in the bulk (see SI7), significantly contribute to the resistivity of the CCO material.

For the Si ( $890 \text{ }\Omega$ ), the unthinned CCO  $\parallel$  ( $430 \text{ }\Omega$ ) and especially for the Mo device ( $186 \text{ }\Omega$ ), which are thick compared to standard TEM specimen thicknesses, the contact resistance is a large contribution to the measured total resistance. In case of the Mo device, a reliable measurement of the conductivity is thus not possible, which would require thinning of the sample to thicknesses below  $100 \text{ nm}$  over an extended area to reach larger resistance values. For the unthinned CCO  $\parallel$  device, the high conductivity ( $\sigma = 5.8 \cdot 10^3 \text{ Sm}^{-1}$ ) is explained by the contribution from the Pt cover. Finally, for the Si device, the calculated resistivity of  $1.3 \cdot 10^{-3} \text{ }\Omega\text{m}$  is considerably lower than the indicated resistivity of the employed Si wafer ( $0.1 \text{ }\Omega\text{m}$ ). This is caused by Ga implantation during FIB milling (approximately  $0.5 \text{ at}\%$ , EDX analysis in SI3), which acts as additional p-doping of the Si, and possibly as well by remaining Pt on the device surface.

## 2.5 Thermoelectric properties

All the studied devices clearly show the induction of a thermovoltage, which increases in magnitude with the temperature gradient created along the material by the differential heating device. The experiments thus prove the possibility to measure thermoelectric properties of materials with the proposed setup. However, for a quantitative analysis, the temperature gradient needs to be known in dependence of the applied heating current  $I_H$ . We performed COMSOL simulations of the temperature distribution under vacuum within the silicon nitride membrane for different  $I_H$  and specimen parameters. Figure 4c and f depict two temperature maps simulated for  $I_H = 5 \text{ mA}$  and assuming a small thermal conductivity of the device material ( $1 \text{ Wm}^{-1}\text{K}^{-1}$ ). The maps illustrate the effect of one important device parameter: the length of the hole milled in the membrane between the contact pads. A short hole, similar in size to the devices analyzed so far, barely affects the temperature distribution in the silicon nitride membrane (left part in Figure 4e), leading to a small temperature difference between the pads. Only a long hole across the entire membrane forms an effective heat barrier and yields a higher temperature (gradient) for the same  $I_H$ , which then merely depends on the thermal conductivity and the geometry of the specimen. To test this simulation result, we milled a longer hole in the membrane of the CCO  $\parallel$  ( $66 \text{ }\mu\text{m}$ ) and the Mo device ( $77 \text{ }\mu\text{m}$ ) and repeated the measurement of the voltage offset in dependence of  $I_H$ . SI13 shows the SEM images of the devices with long hole. The result is plotted in Figure 4d in comparison with the same devices with a short hole and the CCO  $\perp$  device, for which a long hole ( $65 \text{ }\mu\text{m}$ ) was milled directly upon preparation. The measured voltage offset strongly increases by almost two orders of magnitude for the CCO  $\parallel$  device, while the sign changes for the Mo device, which only shows a small change in magnitude. This striking difference is explained by two aspects: the contribution of the Pt contacts and the large difference in thermal conductivity between the two devices. With regard to the first aspect, the contribution of the Pt contacts has been ignored so far. Pt has an absolute Seebeck coefficient ( $-5 \text{ }\mu\text{VK}^{-1}$ ) with the same magnitude as Mo ( $5 \text{ }\mu\text{VK}^{-1}$ ), but with inverted sign. In the device with a short hole, the temperature gradient along both contact paths is largely similar and they cancel each other out almost entirely and the contribution from the Mo device is dominant. In contrast, the temperature gradient along the Pt contacts is asymmetric and their contribution outweighs the contribution of the Mo device for a long hole. Regarding the second aspect, the thermal conductivity is much higher for the metallic Mo ( $139 \text{ Wm}^{-1}\text{K}^{-1}$ ) than for the CCO ( $3 \text{ Wm}^{-1}\text{K}^{-1}$ ) [7]. Therefore, the temperature gradient along the CCO  $\parallel$  device strongly increases, leading to the observed strong increase in the voltage offset. The voltage offset shows an approximate, but not exactly parabolic dependency on  $I_H$ . The deposited power in the heating element is given by  $R_H \cdot I_H^2$ , but  $R_H$  increases with the temperature, adding an additional contribution to the otherwise parabolic relationship. Assuming a linear increase of  $R_H$  with increasing temperature, a valid assumption for Pt in the studied temperature range, the temperature of

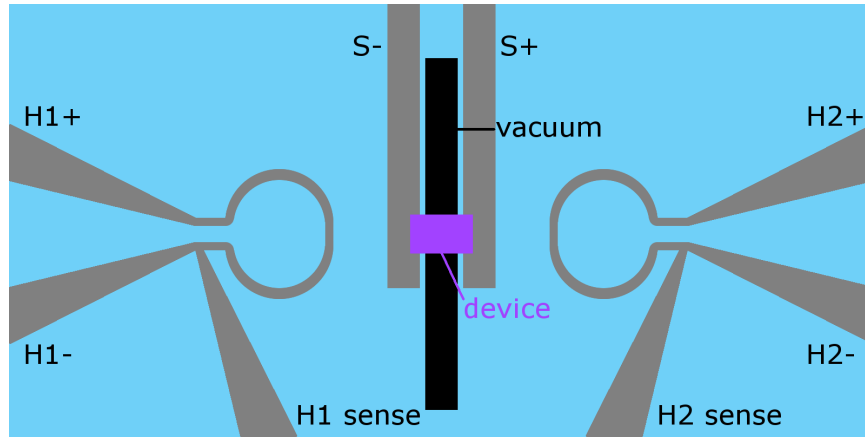


Figure 5: Sketch of the proposed improved chip design for thermoelectric in situ TEM characterization using a holder with eight electrical contacts as detailed in the text. The shown part should be placed on top of a membrane to facilitate the FIB milling of the hole between the contacts.

the heating device  $T_H$  is linearly related to the increase of the heating resistance with respect to its resistance at ambient temperature:  $T_H \propto \Delta R = R_H(T_H) - R_H(T_0)$ . Indeed, when plotting the voltage offset over  $\Delta R$ , a linear dependency is observed (Figure 4e). This indicates that the induced temperature gradient is as well linearly dependent on the temperature of the heating device due to the linear relation between heat flux and temperature gradient. Furthermore, the Seebeck coefficient of the material does not significantly change with temperature in this temperature range, which agrees with bulk studies [7].

The COMSOL simulations indicate that only a hole milled across the whole membrane provides a full prevention of heat flux along the membrane of the chip. However, when opening the hole over the whole membrane, the mechanical tension created along the investigated material that links both sides of the membrane is too large, causing the fracture of the device (SI14).

To get a rough estimation of the value of the Seebeck coefficient of the CCO devices, a value for the temperature gradient needs to be obtained. Therefore, the heater temperature can be calculated from the measured resistance and the calibrated linear temperature coefficient of Pt (SI15), which results in a temperature of approximately 125 and 140°C for the highest applied heating currents for the CCO devices (Figure 4e). Although the COMSOL simulations don't show a quantitative agreement with this estimated temperature, they were used to estimate the ratio between heater temperature and the actual temperature gradient across the device to 3:1 (SI16). Under these assumptions, the Seebeck coefficients of the CCO  $\perp$  and the CCO  $\parallel$  devices are calculated to 135 and 125  $\mu\text{VK}^{-1}$ . Although the values correspond well with bulk values [7], they have to be seen as a very rough estimation and the real values could differ considerably.

## 2.6 Toward fully quantitative thermoelectric characterization

Despite the strong increase in the induced thermovoltage and the good agreement of the estimated Seebeck coefficients, a reliable quantification still requires an exact knowledge of the temperature gradient between the contact pads, which cannot be determined from the employed chip without assuming a value for the thermal conductivity and calculations/simulations of the heat transfer of the device. Due to this limitation, the used chip design is not suitable to fully exploit the advantage of performing thermoelectric measurements by in situ TEM, which would allow studying the interplay between material properties and structure/composition on the local scale.

To reach the possibility of a full quantification, **Figure 5** shows a sketch of a device design, which could facilitate such measurements. The design would require an in situ TEM holder with at least eight electrical contacts. While two contacts would be used for electrical characterization of the device (S-, S+), the remaining six would be designated to two fully symmetrical heating elements. For both, two are used as current supply (H1,2-, H1,2+) and the third one as temperature sensor (H1,2 sense). Temperature

measurement is performed in a three-point setup requiring identical dimensions of the two current paths for the heating elements.

The chip design proposed in Figure 5 considers the following requirements:

- Fully symmetrical layout aiming for a homogeneous temperature distribution and a minimization of potential mechanical tension along the investigated material due to a stress difference between the two sides of the separated membrane.
- Strongly localized heat generation reducing the required length of the hole to form an effective conductivity barrier.
- Possibility to simultaneously control both the sample temperature and the temperature gradient.

The design shown in Figure 5 would have to be placed on top of a silicon nitride membrane. With such a design, it would be possible to determine the temperature gradient and thus to quantify the Seebeck coefficient as well as the conductivity of the studied devices. For example, for the CCO material it would be possible to disentangle the contributions from crystal orientation, grain boundaries or even pores. It is noted that for the employed electron microscope, TEM holders are only available with four contacts. The complete development of a new holder with eight contacts is out of the scope of this work.

### 3 Conclusion

To conclude, our experiments prove that a thermoelectric characterization of micro- and nanosized devices by in situ transmission electron microscopy (TEM) is possible. A thermovoltage is clearly induced in all studied devices and the sign corresponds to the sign of the materials' Seebeck coefficient. The results indicate that the temperature gradient is linearly proportional to the deposited heat energy and that an effective heat barrier should be generated between hot and cold side of the device to obtain a defined temperature gradient along the device. We propose an improved chip design and measurement setup for in situ TEM holders with eight electrical contacts, which should provide the combination of full quantitative thermoelectric characterization with TEM and electron spectroscopies. Such studies will allow to investigate in detail, e.g., the effect of grain boundaries and dopants, in principle down to the single-atom level, on the thermoelectric properties of bulk and nanomaterials. The in situ studies can be further enriched by additional, complementary microscopy techniques performed on the identical device, such as Raman microscopy [24].

## Experimental Section

### *MEMS-based chip fabrication:*

Thermoelectric in situ chips were fabricated by MEMS technology starting with a four-inch 100 Si wafer (380  $\mu\text{m}$  thickness) coated on both sides with 1  $\mu\text{m}$  of low-stress  $\text{SiN}_x$  and following this recipe:

1. Spin coating of Ti35 ESX neg resist (Microchemicals) on the back side with 3000 rounds per minute (rpm).
2. 3 min bake at 100  $^\circ\text{C}$  on hot plate.
3. Optical lithography defining windows for later membrane creation with 175  $\text{mJcm}^{-2}$  and hard contact.
4. 3 min bake at 130  $^\circ\text{C}$  on hot plate.
5. Flood exposure with 520  $\text{mJcm}^{-2}$ .
6. Development for 95s in a 1:1 mixture of  $\text{H}_2\text{O}$  : AZ Developer (Microchemicals).

7. Reactive ion etching (20 sccm SF<sub>6</sub>, 0.19 mbar, 200 W, 15 min) of the back side to remove the SiN<sub>x</sub>.
8. Spin coating of AZ5214E (Microchemicals) with 6000 rpm on the top side.
9. Waiting time of 10 min.
10. 50s bake at 110 °C on hot plate.
11. Optical lithography of front side defining heating element and conductive paths with 26 mJcm<sup>-2</sup> and soft contact.
12. 1 min bake at 120 °C on hot plate.
13. Flood exposure with 390 mJcm<sup>-2</sup>.
14. Development for 35s in AZ 726 MiF (Merck).
15. Sputtering of 5 nm Ti + 150 nm Pt (AJA Orion 5 UHV).
16. Lift-off in acetone assisted by ultrasound.
17. Membrane creation by wet etching in KOH at 80 °C with a holder for front-side protection of the Pt contacts.
18. Cutting of wafer in individual chips by a wafer saw.

#### *Electron microscopy:*

The whole chip is designed to fit in a DENSsolutions Wildfire holder with 4 pins for a ThermoFisher-Scientific/FEI instrument, which allows TEM analysis and electrical characterization of the chip at the same time. TEM, SAED and scanning (S)TEM analysis have been conducted in two aberration-corrected microscopes (Thermo Fisher Scientific Titan<sup>3</sup> (image-corrected) and Titan low-base (probe-corrected)) operated at 300 keV electron energy. Energy-dispersive X-ray spectroscopy (EDX) was performed in STEM mode with an Ultim X-MaxN 100TLE detector (Oxford Instruments).

#### *Bulk CCO material preparation:*

The CCO bulk material was prepared as described in [7] by attrition milling (2h at 600 rpm) starting from SrCO<sub>3</sub>, CaCO<sub>3</sub> and CoO. The mixture was calcinated at 850 °C during 1 h, cold uniaxially pressed into 25 mm diameter disks under 250 MPa, and subjected to hot-uniaxial pressing at 900 °C and 51 MPa for 1 h.

#### *In situ device preparation:*

A dual-beam instrument (Thermo Fisher Scientific Helios 650) with SEM and focused ion beam (FIB) has been utilized to prepare the in situ TEM devices. For bulk materials, FIB-based preparation methods for in situ studies have been published [23] and their first step is the preparation of a conventional TEM lamella: a vertical slice of material with 1 μm thickness, 12 μm width and a depth of approximately 5 μm is taken out from the bulk material and transferred to a TEM copper grid. In a second step, the slice is flipped and transferred to the contact pads of the in situ chip, where a hole has been milled previously between the pads by FIB. The lamella can be thinned prior to transfer to the chip and/or directly on the chip by using a sample holder with inclined surface. Here, we did a combination of both. At first we thinned the sheet on the Cu grid down to 1 μm thickness over the entire width and polished the surface that will be in contact to the chip to guarantee a good contact. Except for the CCO || device, which was transferred without additional pre-thinning, we further thinned the central part of the sheet from one side down to 700 nm forming a kind of bridge. This shape facilitates the thinning after the transfer of the flipped sheet to the chip as it moves the incidence of the focused ion beam away from the surface. The final thinning of the central part and the removal of the Pt cover from the TEM lamella preparation was done using an inclined sample holder that allows milling with the FIB parallel to the chips' surface. SI6 and SI8 describe this preparation for the two CCO samples.

For the MLC NT sample, the preparation needs to be different and we employed a recently developed support-based method [24]. SI10 shows the preparation of the MLC NT device, which consists in first preparing a conventional TEM sample by drop-casting the nanomaterial on a holey silicon nitride chip and the selection of a suitable NT by TEM. Using FIB, the NT and the support are transferred to the in situ chip, where finally the silicon nitride is milled away to leave the NT as unique bridge between the contacts.

#### *Electrical characterization:*

Thermoelectric measurements were performed with two Keithley instruments devices: A Keithley Instruments 2450 SourceMeter (Tektronix) was employed for I-V characterization and a 2611A System Source Meter for simultaneously applying the heating current to the differential heating device.

#### **Supporting Information**

Supporting Information is available from the author.

#### **Acknowledgements**

The authors acknowledge funding from the European Union's Horizon 2020 research and innovation programme under the Marie Skłodowska-Curie grant agreement No 889546 and by the Spanish MCIN (PID2019-104739GB-I00/AEI/10.13039/501100011033 ). The microscopy works have been conducted in the Laboratorio de Microscopias Avanzadas (LMA) at Universidad de Zaragoza. Sample courtesy (MLC NT) from MB Sreedhara and R. Tenne (MLC NT, Weizmann Institute of Science, Israel) is acknowledged. The authors thank M. Rengifo (INMA, Universidad de Zaragoza) for discussions about electrical characterizations, P. Strichovanek (INMA, Universidad de Zaragoza) for Ti-Pt sputter deposition and R. Valero (LMA, Universidad de Zaragoza) for support with MEMS fabrication.

#### **References**

- [1] D. R. Merrill, D. B. Moore, S. R. Bauers, M. Falmbigl, D. C. Johnson, *Materials (Basel, Switzerland)* **2015**, *8*, 4 2000.
- [2] S. Twaha, J. Zhu, Y. Yan, B. Li, *Renewable and Sustainable Energy Reviews* **2016**, *65*, 6 698.
- [3] N. Jaziri, A. Boughamoura, J. Müller, B. Mezghani, F. Tounsi, M. Ismail, *Energy Reports* **2020**, *6*, 7 264.
- [4] Q. Yan, M. G. Kanatzidis, *Nature materials* **2022**, *21*, 5 503.
- [5] A. Nadtochiy, V. Kuryliuk, V. Strelchuk, O. Korotchenkov, P.-W. Li, S.-W. Lee, *Scientific Reports* **2019**, *9*, 1 190.
- [6] J. Jacob, U. Rehman, K. Mahmood, A. Ali, A. Ashfaq, N. Amin, S. Ikram, M. Alzaid, K. Mehboob, *Physics Letters A* **2021**, *388*, 11 127034.
- [7] M. A. Torres, M. A. Madre, O. J. Dura, G. García, S. Marinel, P. Martinez-Filgueira, A. Sotelo, *Ceramics International* **2022**, *48*, 6 7730.
- [8] J. P. Small, K. M. Perez, P. Kim, *Physical review letters* **2003**, *91*, 25 256801.
- [9] K. Fukuhara, Y. Ichinose, H. Nishidome, Y. Yomogida, F. Katsutani, N. Komatsu, W. Gao, J. Kono, K. Yanagi, *Applied Physics Letters* **2018**, *113*, 24 9345.
- [10] Y. Qi, Z. Wang, M. Zhang, F. Yang, X. Wang, *Journal of Materials Chemistry A* **2013**, *1*, 20 6110.
- [11] Y. Liu, M. Zhang, A. Ji, F. Yang, X. Wang, *RSC Advances* **2016**, *6*, 54 48933.
- [12] X. F. Hu, S. J. Li, D. D. Lin, F. Xiong, Z. M. Jiang, X. J. Yang, *Journal of Applied Physics* **2020**, *128*, 18 1457.

- [13] H. Bishara, S. Lee, T. Brink, M. Ghidelli, G. Dehm, *ACS nano* **2021**, *15*, 10 16607.
- [14] S. J. Pennycook, P. D. Nellist, *Scanning Transmission Electron Microscopy: Imaging and analysis*, Springer, New York, NY, **2011**.
- [15] F. L. Deepak, A. Mayoral, R. Arenal, editors, *Advanced Transmission Electron Microscopy*, Springer International Publishing, Cham, **2015**.
- [16] O. L. Krivanek, T. C. Lovejoy, N. Dellby, T. Aoki, R. W. Carpenter, P. Rez, E. Soignard, J. Zhu, P. E. Batson, M. J. Lagos, R. F. Egerton, P. A. Crozier, *Nature* **2014**, *514*, 7521 209.
- [17] X. Yan, C. Liu, C. A. Gadre, L. Gu, T. Aoki, T. C. Lovejoy, N. Dellby, O. L. Krivanek, D. G. Schlom, R. Wu, X. Pan, *Nature* **2021**, *589*, 7840 65.
- [18] Q. Zhang, X. He, J. Shi, N. Lu, H. Li, Q. Yu, Z. Zhang, L.-Q. Chen, B. Morris, Q. Xu, P. Yu, L. Gu, K. Jin, C.-W. Nan, *Nature Communications* **2017**, *8*, 1 4791.
- [19] Y. Sato, T. Gondo, H. Miyazaki, R. Teranishi, K. Kaneko, *Applied Physics Letters* **2017**, *111*, 6 062904.
- [20] P. Nukala, M. Ahmadi, Y. Wei, S. de Graaf, E. Stylianidis, T. Chakraborty, S. Matzen, H. W. Zandbergen, A. Björling, D. Mannix, D. Carbone, B. Kooi, B. Noheda, *Science* **2021**, *372*, 6542 630.
- [21] S. Hettler, D. Sebastian, M. Pelaez-Fernandez, A. M. Benito, W. K. Maser, R. Arenal, *2D Materials* **2021**, *8*, 3 031001.
- [22] S. Hettler, M. B. Sreedhara, M. Serra, S. S. Sinha, R. Popovitz-Biro, I. Pinkas, A. N. Enyashin, R. Tenne, R. Arenal, *ACS nano* **2020**, *14*, 5 5445.
- [23] M. Duchamp, Q. Xu, R. E. Dunin-Borkowski, *Microscopy and microanalysis* **2014**, *20*, 6 1638.
- [24] S. Hettler, M. Furqan, R. Arenal, *Small methods* **2024**, e2400034.
- [25] W. Fulkerson, J. P. Moore, R. K. Williams, R. S. Graves, D. L. McElroy, *Physical Review* **1968**, *167*, 3 765.
- [26] P. Fiffis, L. Kirsch, D. Andruczyk, D. Curreli, D. N. Ruzic, *Journal of Nuclear Materials* **2013**, *438*, 1-3 224.
- [27] Y. Miyazaki, M. Onoda, T. Oku, M. Kikuchi, Y. Ishii, Y. Ono, Y. Morii, T. Kajitani, *Journal of the Physical Society of Japan* **2002**, *71*, 2 491.
- [28] Y. Wang, Y. Sui, J. Cheng, X. Wang, J. Miao, Z. Liu, Z. Qian, W. Su, *Journal of Alloys and Compounds* **2008**, *448*, 1-2 1.
- [29] A. Sotelo, S. Rasekh, G. Constantinescu, M. A. Torres, M. A. Madre, J. C. Diez, *Ceramics International* **2013**, *39*, 2 1597.
- [30] D. B. Strukov, G. S. Snider, D. R. Stewart, R. S. Williams, *Nature* **2008**, *453*, 7191 80.